Three-axis isotropic-sensitivity ^{4}He magnetometer with alignment-based longitudinal parametric resonance

Bowen Wang, Xiang Peng,* Wei Xiao, and Hong Guo†
State Key Laboratory of Advanced Optical Communication Systems and Networks, School of Electronics, and Center for Quantum Information Technology, Peking University, Beijing 100871, China

(Received 19 September 2022; accepted 28 November 2022; published 12 December 2022)

For measurements in near-zero magnetic fields, vector atomic magnetometers are promising alternatives to scalar versions, but generally suffer from inconsistent performance over three axes. We present a single-beam vector magnetometer with three-axis isotropic sensitivity based on ^{4}He atomic alignment. Longitudinal parametric resonance with atoms pumped by linearly polarized light is proposed for the z-axis measurement, while the Hanle effect in transverse geometry is used for x- and y-axis measurements. The evolution of atomic alignment multipole components and expressions of the three-axis magnetic responses are analyzed in detail. We describe the experimental operation of the proposed magnetometer with a magnetic-field noise floor of 150 $\mathrm{fT/Hz^{1/2}}$ for the three axes, which is attractive for biomagnetism requiring vector characterization and source reconstruction.

DOI: 10.1103/PhysRevA.106.063102

I. INTRODUCTION

Optically pumped atomic magnetometers play a significant role in biomagnetic imaging [1], fundamental physics [2], geophysics [3], and space science [4]. Such magnetometers are typically classified into one of two categories: scalar and vector atomic magnetometers (VAMs) [5]. Scalar atomic magnetometers read the Larmor frequency of magnetooptical resonance driven by the radio-frequency (rf) field [6] or modulated light [7]. VAMs have the ability to sense the magnetic-field components in three-dimensional coordinates, and they aroused intense interest, especially in near-zero magnetic-field measurements [8–10].

One of the intrinsic mechanisms of VAMs based on zero-field resonance is the Hanle effect [11,12]. Hanle magnetometers survey magnetic fields by detecting the magnetically induced polarization degradation or absorption variation of a laser beam transmitted through an atomic cell [13,14]. Parametric resonance technique is implemented by applying nonresonant rf fields to the polarized atomic ensemble on the basis of a Hanle magnetometer [15,16], and the atoms are considered to be dressed by "rf photons" [17,18]. In addition, parametric-resonance magnetometers (PRMs) suppress low-frequency noise by carrying the signal to the rf range [19,20].

PRMs have long been designed with a transverse field geometry in which the rf fields are set perpendicular to the atomic polarization. Three-axis PRMs with two transverse rf fields were reported, both in theoretical modeling [21,22] and experimental implementation [23,24]. These dual-rf PRMs were used in research on magnetoencephalography [25] and magnetocardiography [26]. However, both orientation- and alignment-based transverse PRMs can only ensure the proper sensitivity in two axes of the rf field directions, with the third axis usually suffering from unsatisfactory performance [27,28].

Longitudinal field modulation along the direction of atomic orientation polarization is an alternative means of inducing parametric resonance [29]. To provide orientation-based longitudinal PRMs with the capability of dual- or three-axis measurements, an additional probe beam is usually applied [30,31]. Similar to transverse PRMs, conventional longitudinal PRMs also suffer from anisotropic sensitivity [32]. Three-axis isotropic sensitivity of 500 $\mathrm{fT/Hz^{1/2}}$ was achieved in a dual-rf PRM through a combination of atomic orientation and alignment [33], but the vector-light-shift noise caused by the orientation part limits the sensitivity. Thus, a pure alignment-based scheme with isotropic sensitivity is worthy of study.

In this article, we present a zero-field VAM with three-axis isotropic sensitivity based on ^{4}He alignment. Longitudinal parametric resonance with atoms pumped by linearly polarized light is proposed for z-axis measurements, and the magnetic fields along the x and y axes are measured using the Hanle effect in the transverse geometry. With the combination of these two geometries, the three magnetic-field components are simultaneously demodulated from the detected absorption of a single pump beam. The evolution of alignment multipole components and analytical expressions of the three-axis magnetic responses are obtained. We experimentally demonstrate the magnetometer with three-axis isotropic sensitivity after optimizing the modulation field parameters. The operation of the ^{4}He gas cell does not require heating or cryogenic cooling, making the proposed magnetometer highly suitable in biomagnetic applications.

The remainder of this paper is organized as follows. In Sec. II, we describe the theoretical model from single- to three-axis geometry and derive analytical expressions for photodetection signals. Section III demonstrates the experimental

*xiangpeng@pku.edu.cn
†hongguo@pku.edu.cn

 ©2022 American Physical Society

setup, magnetic responses, and working performance of the proposed magnetometer. Finally, we conclude this paper in Sec. IV by discussing the characteristics and merits of our three-axis ^{4}He magnetometer.

II. THEORETICAL MODEL

We derive analytical expressions for the zero-field resonance profiles of longitudinal parametric resonance in the z axis and the transverse Hanle effect in the x and y axes with a linearly polarized pump beam. The "three-step approach" [34] is adopted to analyze the evolution of alignment multipole components under the low light power limit. The three steps are composed of optical-pumping preparation, magnetic-field-induced evolution, and photoelectric detection of the atomic polarization. Note that the second-order effects caused by high light power, such as anisotropic relaxation and alignment-to-orientation conversion in parametric resonance [35], are not considered here. In addition, the quantization axis is defined along the polarization axis of the linearly polarized pump beam.

The density matrix $\hat{\rho}$ describes the atomic ensemble with angular momentum F and reflects the dynamics of the magnetometer system. This matrix can be expanded into the irreducible tensor operator basis [36]

$$\hat{\rho} = \sum_{k=0}^{2F}\sum_{q=-k}^{+k} m_q^{(k)}\hat{T}_q^{(k)\dagger} = \sum_{k=0}^{2F}\sum_{q=-k}^{+k} m_q^{(k)}(-1)^q\hat{T}_{-q}^{(k)}, \tag{1}$$

where $\hat{T}_q^{(k)}$ is the qth component of the irreducible tensor operator of order k, with $q = -k, -k+1, \ldots, k-1, k$. The matrix elements of each $\hat{T}_q^{(k)}$ in the case of metastable ^{4}He are given in Ref. [37]. The atomic multipole moments $m_q^{(k)} = \mathrm{Tr}(\hat{\rho}\hat{T}_q^{(k)})$ contain the full information of $\hat{\rho}$ and determine the photodetection signals. For $F = 1$ metastable ^{4}He, the electric dipole interaction between light and atoms involves three kinds of atomic multipole moments, namely, the $m_0^{(0)}$ population term, $m_q^{(1)}$ orientation terms, and $m_q^{(2)}$ alignment terms. Neglecting alignment-to-orientation conversion, the linearly polarized light only couples the five alignment multipole components, which are usually written as a column matrix for convenience

$$M = \left(m_{-2}^{(2)}, m_{-1}^{(2)}, m_0^{(2)}, m_1^{(2)}, m_2^{(2)}\right)^{\mathrm{T}}. \tag{2}$$

A. Single-axis geometry with static driving field

We present the single-axis geometry in Fig. 1(a) to explain the alignment-based longitudinal parametric resonance. An ensemble of metastable ^{4}He atoms is interrogated by the linearly polarized light resonating with the D_0 ($2\,^3S_1 \rightarrow 2\,^3P_0$) transition. The light polarization $\vec{\epsilon}$ is directed along the z axis, which we call z-polarized light in the following. In the z axis, an oscillating rf field $B_1\cos\omega t$ with amplitude B_1 and frequency ω is applied to dress the atoms with "rf photons," i.e., to induce parametric resonance. We expect to measure the magnetic field along the z axis, but the spin polarization does not precess because it is parallel to all the fields. Therefore, a transverse driving field B_m in the x-y plane must be introduced to induce the evolution of observables. Setting the direction of the static driving field to any direction within the transverse plane is equivalent because the field geometry is rotationally symmetric along the z axis before this field is applied. We define this geometry as alignment-based longitudinal parametric resonance, as its rf field is applied along the axis of atomic alignment polarization. In the following derivations, we consider the example of the static driving field B_m directed along the x axis to formulate the definite expressions.

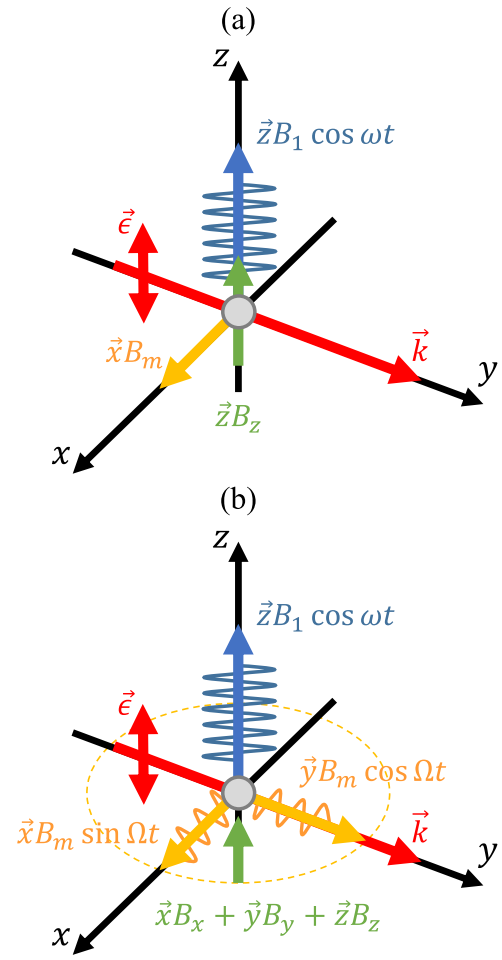

FIG. 1. (a) Single-axis and (b) three-axis geometries of the alignment-based zero-field ^{4}He vector magnetometer with longitudinal parametric resonance. $\vec{i}B_i(i = x, y, z)$, components of quasistatic field to be measured; B_1, amplitude of the rf dressing field with frequency ω; B_m, amplitude of the static driving field in single-axis geometry or the rotating driving field with frequency Ω in three-axis geometry; $\vec{k}$, light propagation; $\vec{\epsilon}$, light polarization. The spheres at the center of the coordinates represent atomic ensembles.

The quantum Liouville equation illustrates the dynamics of the 3×3 density matrix for metastable ^{4}He [22]:

$$\frac{d\hat{\rho}}{dt} = -i[\hat{H}(t), \hat{\rho}(t)] + \Gamma[\hat{\rho}_s - \hat{\rho}(t)], \tag{3}$$

where $\hat{H}(t) = -\gamma\vec{B}\cdot\hat{F}$ is the Zeeman Hamiltonian, $\gamma = -2\pi \times 28.025$ Hz/nT is the gyromagnetic ratio of metastable ^{4}He, and $\vec{B} = \vec{x}B_m + \vec{z}(B_z + B_1\cos\omega t)$ is the total magnetic field in the single-axis geometry. Γ is the total relaxation, and $\hat{\rho}_s$ is the steady-state density matrix prepared by the combined

action of optical pumping and relaxation, that is, the first step in the three-step approach. In the case of z-polarized light, $\hat{\rho}_s$ is expressed as [38]

$$\hat{\rho}_s = \frac{1}{3\Gamma}\begin{pmatrix} \Gamma_e + (3/2)\Gamma_p & 0 & 0 \\ 0 & \Gamma_e & 0 \\ 0 & 0 & \Gamma_e + (3/2)\Gamma_p \end{pmatrix}, \tag{4}$$

where Γ_e is the metastable atom collision relaxation, Γ_p is the optical pumping relaxation, and the total relaxation rate is $\Gamma = \Gamma_e + \Gamma_p$, which is on the order of kHz for the ^{4}He gas cell used in the subsequent experiments. According to the known $\hat{T}_q^{(2)}$, the steady-state multipole moments column matrix is calculated as

$$M_s = \left(0, 0, \frac{\Gamma_p}{\sqrt{6}\Gamma}, 0, 0\right)^{\mathrm{T}}. \tag{5}$$

Using the Racah commutator relations between angular momentum components and irreducible tensor operators, Eq. (3) can be further written as an evolution equation of multipole components

$$\left[\frac{d}{dt} - I(\vec{B}) + \Gamma\right]M = \Gamma M_s, \tag{6}$$

where $I(\vec{B})$ describes the interactions between the five alignment multipole components and magnetic fields. This 5×5 matrix is given by

$$I(\vec{B}) = \begin{pmatrix} -2\Delta & B_m & 0 & 0 & 0 \\ B_m & -\Delta & \sqrt{3/2}B_m & 0 & 0 \\ 0 & \sqrt{3/2}B_m & 0 & \sqrt{3/2}B_m & 0 \\ 0 & 0 & \sqrt{3/2}B_m & \Delta & B_m \\ 0 & 0 & 0 & B_m & 2\Delta \end{pmatrix}, \tag{7}$$

where $\Delta = B_z + B_1 \cos\omega t$. Under a time-dependent rf field, it is difficult to solve Eq. (6) for nontrivial solutions. Therefore, we employ the dressed-atom formalism developed by Cohen-Tannoudji *et al.* [39]. In this formalism, the rf field is quantized to the Fock state with a certain number of "rf photons" to eliminate the time dependence of the Hamiltonian. Under rf-field dressing, an infinite number of harmonics appear in the evolution of spin polarization. When the rf photon number is much greater than 1, the dressed-atom formalism implies that the parametric resonance can be mapped into the Hanle effect of dressed atoms by [40]

$$m_q^{(2)} = \bar{m}_{\mathrm{Hanle},q}^{(2)} \exp\left(iq\frac{\gamma B_1}{\omega}\sin\omega t\right) = \bar{m}_{\mathrm{Hanle},q}^{(2)} \sum_{p=-\infty}^{\infty} J_{p,q} e^{ip\omega t}, \tag{8}$$

where $J_{p,q} = J_p(q\gamma B_1/\omega)$ is the pth order Bessel function of the first kind from the Jacobi-Anger expansion and $\bar{m}_{\mathrm{Hanle},q}^{(2)}$ is the Hanle effect solution subject to the dressed magnetic-field components

$$\bar{B}_z = B_z, \tag{9a}$$

$$\bar{B}_{x,y,m} = J_{0,1}B_{x,y,m}. \tag{9b}$$

We substitute the Hanle effect solution shown in the Appendix [see Eq. (A2)] into Eq. (8), and then use Euler's formula before extracting the first-harmonic term. The evolutions of the multipole components, i.e., the second step, in alignment-based longitudinal parametric resonance are then obtained as

$$m_0^{(2)} = \frac{\Gamma_p\left[\left(\Gamma^2 - 2\omega_z^2 + J_{0,1}^2\omega_m^2\right)^2 + 9\omega_z^2\Gamma^2\right]}{\sqrt{6}\Gamma\left(\omega_z^2 + J_{0,1}^2\omega_m^2 + \Gamma^2\right)\left(4\omega_z^2 + 4J_{0,1}^2\omega_m^2 + \Gamma^2\right)}, \tag{10a}$$

$$m_2^{(2)} = -\frac{J_{1,2}J_{0,1}^2\omega_m^2\Gamma_p\left(i\Gamma^2 - 2i\omega_z^2 + iJ_{0,1}^2\omega_m^2 + 3\omega_z\Gamma\right)}{\Gamma\left(\omega_z^2 + J_{0,1}^2\omega_m^2 + \Gamma^2\right)\left(4\omega_z^2 + 4J_{0,1}^2\omega_m^2 + \Gamma^2\right)} \times \sin\omega t, \tag{10b}$$

$$m_1^{(2)} = \frac{J_{1,1}J_{0,1}\omega_m\Gamma_p\left(\Gamma^2 - 2\omega_z^2 + J_{0,1}^2\omega_m^2 - 3i\omega_z\Gamma\right)}{\Gamma\left(\omega_z^2 + J_{0,1}^2\omega_m^2 + \Gamma^2\right)\left(4\omega_z^2 + 4J_{0,1}^2\omega_m^2 + \Gamma^2\right)} \times (2i\omega_z + \Gamma)\sin\omega t, \tag{10c}$$

$$m_{-2}^{(2)} = m_2^{(2)*}, m_{-1}^{(2)} = -m_1^{(2)*}, \tag{10d}$$

where $\omega_{z,m} = -\gamma B_{z,m}$. In Eq. (10), $m_0^{(2)}$ is a time-independent component representing the Hanle effect contained in the PRM, and the other four components oscillate at a frequency of ω. The significance of the static driving field B_m can thus be understood from Eq. (10). If we let $\omega_m = 0$, then $m_{\pm2}^{(2)} = m_{\pm1}^{(2)} = 0$ and $m_0^{(2)} = \Gamma_p/\sqrt{6}\Gamma$, which are the steady-state multipole moments illustrated in Eq. (5). That is, the multipole components will remain at the first step without any evolution if there is no driving field in the transverse plane.

The third step, i.e., photoelectric detection, involves extracting the magnetic-field response of the atomic medium from its multipole moments. Considering linearly z-polarized light, the light absorption, i.e., response of the magnetometer in the single-axis geometry, depends on [41]

$$R_z = \alpha\Gamma' I_0\left(\frac{1}{\sqrt{3}}m_0^{(0)} + \frac{1}{\sqrt{6}}m_0^{(2)} + \mathrm{Re}\left(m_2^{(2)}\right)\right), \tag{11}$$

where the constant α is proportional to the optical thickness of the atomic cell, Γ' is the light-induced broadening, and I_0 is the incident light intensity. Note that the population term $m_0^{(0)}$ is usually neglected because it does not carry magnetic-field information. In addition, the time-independent DC term $m_0^{(2)}$ will be filtered out by the practical lock-in detection without additional dither modulation. Therefore, the zero-field parametric-resonance response of the single-axis geometry completely depends on the real part of $m_2^{(2)}$, the theoretical amplitude of which is shown in Fig. 2(a). It has a zero-crossing dispersive line shape suitable for near-zero magnetic-field measurements.

Note that we only discuss the zero-field resonance signal in the present context and the high-order resonances occurring at the integral multiple of the rf-field frequency are not considered, nor are they used in the subsequent experimental measurements.

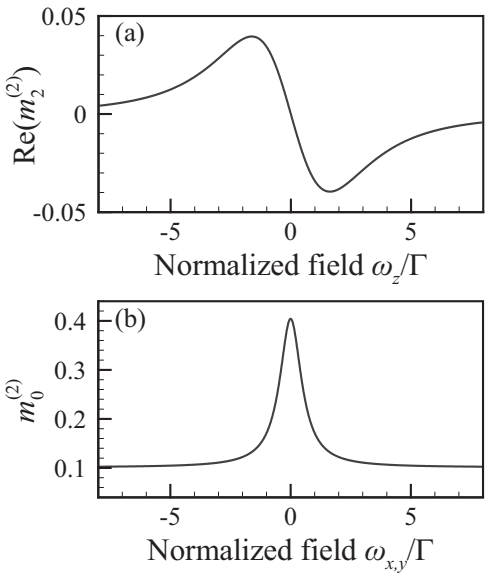

FIG. 2. Theoretical amplitudes of the relevant multipole moments: (a) real part of $m_2^{(2)}$ versus longitudinal quasistatic field normalized to ω_z/Γ; (b) $m_0^{(2)}$ versus transverse quasistatic fields normalized to $\omega_{x,y}/\Gamma$. The rf-field parameters in the simulations are $B_1 = 72$ nT and $\omega = 2\pi \times 3333$ Hz.

B. Three-axis geometry with rotating driving field

The measurement capabilities of the x and y axes can be realized by introducing the Hanle effect of transverse geometry, using a rotating driving field with relatively low frequency to replace the static driving field. If the same amplitude B_m as the static driving field is maintained, the rotating driving field in the transverse plane does not substantially change the longitudinal parametric resonance in the z axis, with the signal carried to a higher frequency by the rf dressing field.

Figure 1(b) shows the three-axis geometry of our magnetometer. The rotating driving field is realized by applying dither modulations $B_m \sin \Omega t$ along the x axis and $B_m \cos \Omega t$ along the y axis simultaneously. In addition, the condition $\Omega \ll \omega$ is required to ensure that the Hanle resonance in the x-y plane can be extracted without disturbing the longitudinal parametric resonance in the z axis. Considering the $\pi/2$ phase difference between the two dither modulations, the x-axis response is sensitive to the in-phase component, while the y-axis response is sensitive to the quadrature component in the lock-in detection with a demodulation frequency of Ω.

We investigate the Hanle effect term, i.e., Eq. (10a), when the transverse quasistatic field is swept to explain the resonance in the x-y plane. For the rotationally symmetric geometry, we take the magnetic-field response of the x axis as an example; the response of the y axis is similar to that of the x axis. In Eq. (10a), we set $\omega_z = 0$ and rewrite ω_m to ω_x with $\omega_x = -\gamma B_x$ to give (no driving field is introduced at present)

$$m_0^{(2)}(\omega_x) = \frac{\Gamma_p\left(J_{0,1}^2\omega_x^2 + \Gamma^2\right)}{\sqrt{6}\Gamma\left(4J_{0,1}^2\omega_x^2 + \Gamma^2\right)}. \tag{12}$$

From Eq. (12), the typical Hanle resonance in transverse geometry is theoretically obtained by sweeping B_x around the zero field, as shown in Fig. 2(b). After the rotating driving field is applied, the evolution of the Hanle effect term $m_0^{(2)}(\omega_x)$ along the x axis becomes the time-dependent $m_0^{(2)}(\omega_x + \omega_m \sin \Omega t)$. The demodulated x-axis response R_x is obtained by the standard lock-in detection process: the original oscillating signal is multiplied by a normalized reference signal $\sin \Omega t$, and the DC term is extracted by a low-pass filter. This process is described algebraically as

$$\begin{aligned} R_x &= \frac{1}{T}\int_0^T \sin(\Omega t) m_0^{(2)}(\omega_x + \omega_m \sin \Omega t)dt \\ &= -\frac{\sqrt{6}J_{0,1}^2\Gamma_p\Gamma\omega_m\omega_x}{2\left(\Gamma^2 + 4J_{0,1}^2\omega_x^2\right)^2}, \end{aligned} \tag{13}$$

where $T = 2\pi/\Omega$ and the Taylor expansion is used in the calculation. Equation (13) exhibits a dispersive line shape with a negative zero-crossing slope; the y-axis response R_y has a similar expression and can be obtained in the same way. Overall, the demodulated magnetic-field responses in all three axes manifest a zero-field dispersive resonance in theory, based on which our magnetometer can be reasonably implemented.

III. EXPERIMENTS AND DISCUSSION

A. Experimental setup

We implemented the proposed three-axis ^{4}He magnetometer in a laboratory environment. A schematic diagram of the implementation is shown in Fig. 3. A 1083.206-nm resonant pump beam was emitted from a fiber laser (NKT Koheras BOOSTIK Y10), and the laser power was stabilized by a customized noise eater composed of an acoustooptic modulator, proportional-integral-derivative controller, and photodiode. The waist diameter of the Gaussian pump beam was expanded to 12 mm ($1/e^2$) by a beam expander, and a half-wave plate was used to adjust the light intensity in conjunction with the subsequent polarizer, which applied polarization along the z axis. Next, the linearly z-polarized light entered the gas cell, which was located in a seven-layer mu-metal magnetic shield. The cylindrical cell (50-mm diameter and 70-mm length) was filled with 0.57 Torr of ^{4}He before undergoing an electrodeless discharge at frequency 39.59 MHz. The power consumption for electrodeless-discharge rf excitation was 112 mW, and the rf power absorbed by the ^{4}He gas cell was 100 mW. Thus, part of the ^{4}He gas was populated from the ground state $1\,^1S_0$ to the metastable state $2\,^3S_1$. The absorption of the pump beam was measured by a customized indium gallium arsenide (InGaAs) photodiode, and the photocurrent was processed by a low-noise AC-coupled amplifier (FEMTO Messtechnik DLPCA-200) with the gain of 10^6 V/A. In addition, the intensity of the pump beam before entering the gas cell was optimized to 0.6 mW according to the signal amplitude on the photodiode. This single-beam optical setup is conducive to the miniaturization of the magnetometer.

Regarding the electrical configuration, a function generator embedded in the lock-in amplifier (Zurich Instruments HF2LI) generated two modulations: (i) the rf field at a frequency of $\omega = 2\pi \times 3333$ Hz in the z axis for longitudinal parametric resonance and (ii) the rotating field at a frequency

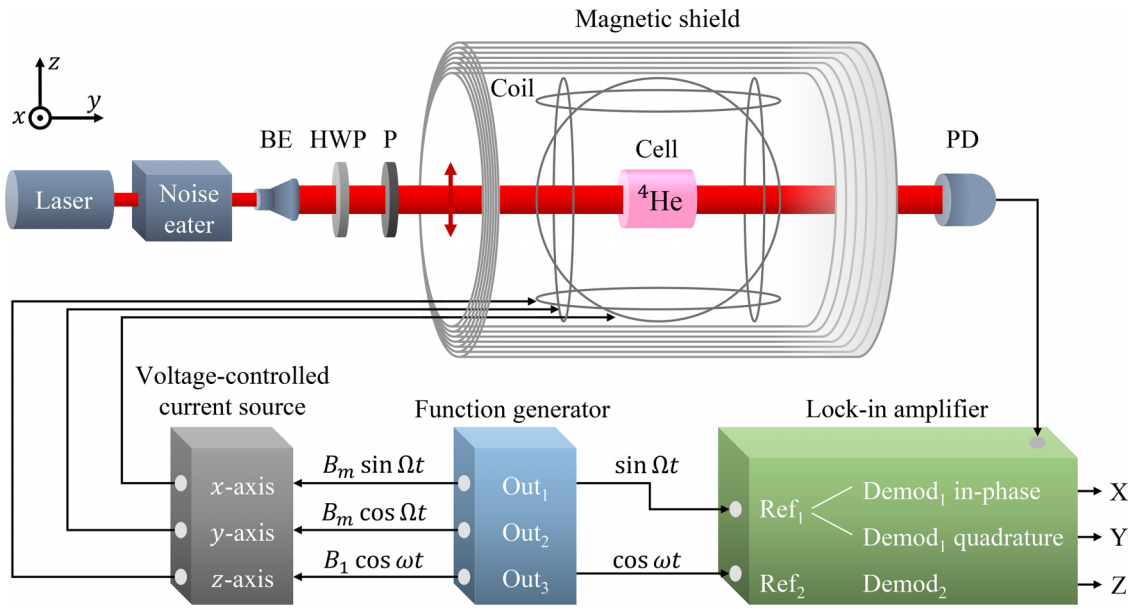

FIG. 3. Schematic diagram of the three-axis ^{4}He magnetometer with alignment-based longitudinal parametric resonance. BE, beam expander; HWP, half-wave plate; P, polarizer; PD, photodiode.

of $\Omega = 2\pi \times 737$ Hz in the x-y plane for the transverse Hanle effect. These two modulation frequencies were selected according to the signal-to-noise ratios of the demodulated signals. All applied modulations were converted into currents by voltage-controlled current sources (Stanford Research Systems CS580) and injected into a three-axis Helmholtz coil. The coil constant was calibrated *in situ* using the parametric-resonance method described in Ref. [42]. On the other side, the magnetically induced absorption signals were demodulated at the first harmonic by the lock-in amplifier with two demodulators. Demodulator-1 took $\sin \Omega t$ as the reference signal, with the demodulated in-phase component describing the x-axis magnetic response and the quadrature component giving the y-axis magnetic response. The reference frequency of demodulator-2 was ω, and the z-axis magnetic response was read from either the in-phase or quadrature component, depending on the demodulation phase settings. Interestingly, the magnetic responses of the three axes can be obtained simultaneously by only two demodulators. According to the calibrated zero-crossing slopes of the magnetic responses, the values of the magnetic fields in the x, y, and z axes were read out at a sampling rate of 14.39 kHz.

Because the proposed magnetometer is based on light-absorption detection, the laser intensity noise affects the sensitivity of the magnetometer and needs to be properly treated. After the proportional-integral-derivative parameters of the customized noise eater were tuned on the basis of the Ziegler-Nichols method, the relative intensity noise floor of the pump beam was optimized to -132 dBc/Hz.

B. Three-axis magnetic responses

The magnetic responses of three axes were experimentally obtained by scanning the quasistatic fields ranging from -150 nT to 150 nT in the corresponding axes during demodulation. The peak-to-peak amplitudes of the zero-field resonance increase with the amplitudes of the applied modulation fields and the linewidths are also broadened. Both effects influence the zero-crossing slopes. First, the amplitude of the rf dressing field was chosen to be $B_1 = 72$ nT to obtain a considerable parametric-resonance profile. Next, we modified the amplitude of the rotating driving field according to the absolute values of the linearly fitted zero-crossing slopes of the magnetic responses in the three axes, as shown in Fig. 4. The maximum absolute values of the slopes for the x and y axes occurred with a rotating-field amplitude of 18 nT, but this operating point resulted in an extremely weak z-axis parametric-resonance slope. Fortunately, when $B_m = 48$ nT, at the expense of some degradation in the slopes of the x and y axes, we obtained the largest absolute value of the

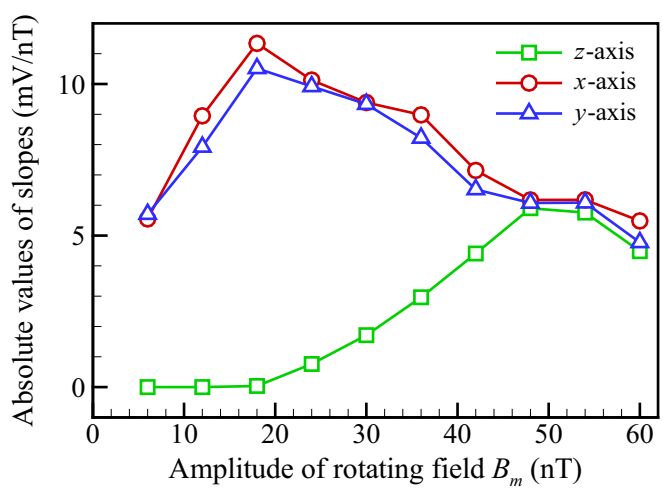

FIG. 4. Absolute values of linearly fitted zero-crossing slopes of the magnetic responses. The green line with squares, red line with circles, and blue line with triangles show the z-, x-, and y-axis slopes, respectively, for different amplitudes of the rotating driving field.

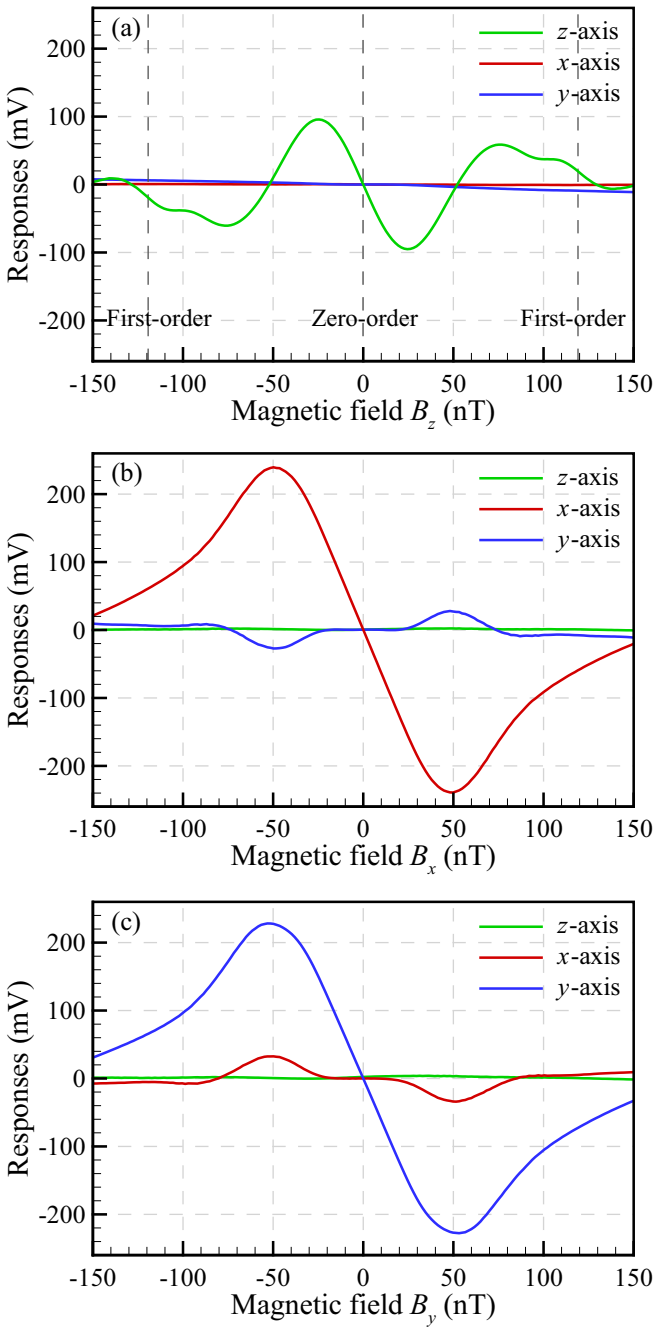

FIG. 5. Magnetic responses of the three-axis ^{4}He magnetometer with alignment-based longitudinal parametric resonance when the quasistatic fields were scanned along the (a) z, (b) x, and (c) y axis. The green, red, and blue plots manifest the z-, x-, and y-axis responses, respectively.

z-axis slope and made the zero-crossing slopes of the three axes almost uniform. To ensure that our magnetometer has isotropic sensitivity, the amplitude of the rotating driving field was therefore selected to be this compromised value.

The subsequent magnetic responses of the three axes are shown in Fig. 5. For the z axis, the zero- and first-order parametric resonances occur at $B_z = 0$ and $B_z = \pm\omega/\gamma = \pm 119$ nT, respectively. The zero-order parametric resonance has a peak-to-peak amplitude of 191 mV and a linewidth of 49 nT. Although the first- and higher-order parametric resonances have the potential to measure finite magnetic fields, we do not use them for measurements because their dispersion center points are generally not at zero voltage and they have relatively small resonance slopes. Note that we also performed this experiment using the single-axis geometry (results not shown), and found that the zero-field resonance coincided well with the green plot in Fig. 5(a). This agreement validates the analysis of the field geometry, that is, whether the driving field is static or rotating does not intrinsically affect the longitudinal parametric resonance in the z axis.

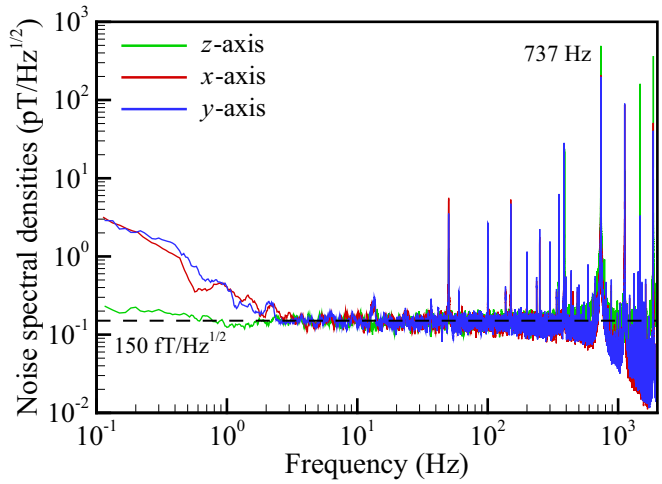

FIG. 6. Noise spectral densities of the three-axis ^{4}He magnetometer with alignment-based longitudinal parametric resonance. The magnetic-field noise floors are 150 fT/Hz$^{1/2}$ for the x (red plot), y (blue plot), and z axes (green plot).

In Fig. 5(b), the x-axis response exhibits a first-derivative demodulated Hanle resonance with a peak-to-peak amplitude of 479 mV and a linewidth of 100 nT. In Fig. 5(c), the y-axis response curve has a peak-to-peak amplitude of 455 mV and a linewidth of 106 nT. Section II predicted that the x- and y-axis responses would only be sensitive to the in-phase and quadrature components of the demodulation, respectively. Our experiments found almost no response in the y axis around the zero field when scanning B_x, and vice versa when B_y was swept. In addition, the characteristics of the x- and y-axis responses when the quasistatic field was scanned in their respective directions should theoretically be the same. However, the experimental results present some differences in amplitude or linewidth because there were slight differences in the fields actually experienced by the atomic ensemble in the two directions.

It is remarkable that the peak-to-peak amplitude of the zero-field parametric resonance in the z axis is evidently smaller than that of the Hanle resonance in the x and y axes. Nonetheless, the zero-crossing slopes of the responses of the three axes can still be optimized so that they are similar to each other because the linewidth of the longitudinal parametric resonance is narrower than that of the transverse Hanle resonance. The amplitude difference between the parametric resonance and Hanle resonance can be explained by their respective analytical expressions. As can be seen from the real part of Eq. (10b), the amplitude of the alignment-based longitudinal parametric resonance is

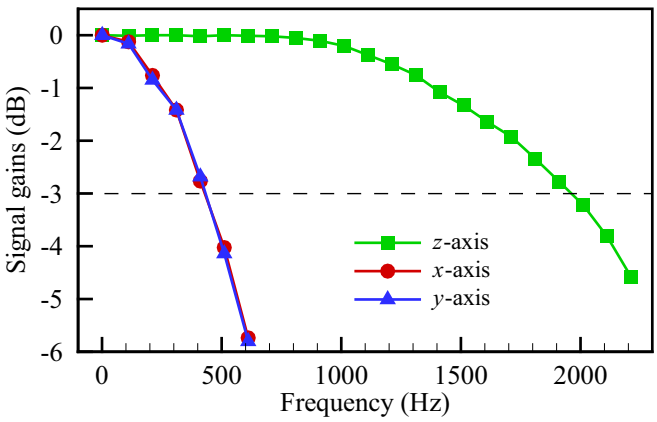

FIG. 7. Frequency responses of the three-axis ^{4}He magnetometer with alignment-based longitudinal parametric resonance. The green plot illustrates a z-axis bandwidth of 1960 Hz. The red and blue plots demonstrate the bandwidths of 430 Hz for the x and y axes.

constrained by a first-order Bessel function of the first kind, $J_{1,2}$, the maximum value of which does not exceed 0.582, while the theoretical amplitude of the Hanle resonance is not damped by the coefficient $J_{1,2}$; see Eq. (13).

The theoretical fitting (not shown) of the experimentally observed three-axis responses was performed, but there were slight differences between the fitting results and the experimental values due to the theoretical approximations at the beginning of Sec. II. The modified model that takes the second-order effects into account is our future research interest.

C. Performance analysis

After the magnetic-field responses were obtained, we shifted the low-pass filter bandwidth of the lock-in amplifier to 500 Hz for demodulator-1 and 2000 Hz for demodulator-2. Then, we read the magnetic fields from the demodulated voltages according to the calibrated linear regions of the dispersive curves. Figure 6 illustrates the noise spectral densities of the magnetometer calculated from a set of magnetic-field data in 60-s duration time. When recording the noise spectral densities, the parameters of pump beam, rf dressing field, and rotating driving field were the same as those when recording the data of Fig. 5. The sensitivities are $150\,\mathrm{fT/Hz^{1/2}}$ for the three axes. Additionally, the spikes in the noise spectral densities are caused by the power frequency and harmonics of the modulation frequency.

As for the bandwidths of the magnetic-field measurements, the frequency responses were obtained by applying a sinusoidal field with an amplitude of 6 nT at different frequencies, as shown in Fig. 7. The -3 dB bandwidth is 1960 Hz for the z axis and 430 Hz for the x and y axes. The difference in bandwidth is due to the distinct low-pass filter settings of the two demodulators, which depend on the modulation frequency of the corresponding axis.

Considering the orthogonality between the three axes of our magnetometer, the magnetic-field leakages between axes were measured by applying a sinusoidal field with a frequency of 1 Hz to one axis and then recording the response amplitudes of the other two axes. The results indicate that the three-axis ^{4}He magnetometer suffers 0.5% and 3.0% leakages into B_y and B_z, respectively, when applying the B_x field, 0.5% and 8.4% leakages into B_x and B_z, respectively, when applying the B_y field, and 3.4% and 0.4% leakages into B_x and B_y, respectively, when applying the B_z field. The magnetic-field leakage between the x and y axes was significantly reduced by precisely setting the demodulation phase, while the leakages between the transverse axes and the z axis could be further suppressed by modifying the design of the coil framework. In addition, the nonlinear nature of magnetic response is also a potential factor causing field leakages.

The performance of the proposed magnetometer is sufficient for biomagnetic measurements, such as for magnetocardiography and magnetoencephalography. In the future, a spherical or cubic ^{4}He gas cell and corresponding discharge scheme will be designed to improve the consistency between the x- and y-axis responses. Due to the presence of the AC modulation fields in our magnetometer, the crosstalk among magnetometers should be carefully addressed by data postprocessing or an all-optical structure in the integrated multisensor design.

IV. CONCLUSION

In conclusion, we presented a three-axis isotropic-sensitivity ^{4}He magnetometer. The magnetic field along the z axis was obtained by the proposed longitudinal parametric resonance based on linearly polarized light pumping, and the Hanle effect in the transverse geometry was used to measure the magnetic fields along the x and y axes. With only two demodulators, the magnetic responses of the three axes were extracted from the absorption of the pump beam. The evolution of the alignment multipole moments in the polarized ^{4}He ensemble was algebraically analyzed, and we obtained analytical expressions for the three-axis magnetic responses. The proposed magnetometer was experimentally operated at room temperature without heating or cryogenic cooling. An isotropic sensitivity of $150\,\mathrm{fT/Hz^{1/2}}$ was obtained for the three axes and the bandwidths were 430 Hz, 430 Hz, and 1960 Hz for the x, y, and z axes, respectively. Our magnetometer has a single-beam optical setup, which is important for the integration of magnetometers in biomagnetic applications.

ACKNOWLEDGMENTS

This work was supported by the National Natural Science Foundation of China (Grants No. 61571018 and No. 61531003).

APPENDIX

This Appendix derives the steady-state solution of the alignment-based longitudinal Hanle effect in metastable ^{4}He atoms. By temporarily neglecting the oscillating term in Δ,

Eq. (6) can be written as

$$\frac{d}{dt}m_0^{(2)} + i\gamma\left[\sqrt{3/2}B_m m_{-1}^{(2)} + \sqrt{3/2}B_m m_1^{(2)}\right] + m_0^{(2)}\Gamma = \frac{\Gamma_p}{\sqrt{6}}, \tag{A1a}$$

$$\frac{d}{dt}m_{\pm 2}^{(2)} + i\gamma\left[\pm 2B_z m_{\pm 2}^{(2)} + B_m m_{\pm 1}^{(2)}\right] + m_{\pm 2}^{(2)}\Gamma = 0, \tag{A1b}$$

$$\frac{d}{dt}m_{\pm 1}^{(2)} + i\gamma\left[B_m m_{\pm 2}^{(2)} \pm B_z m_{\pm 1}^{(2)} + \sqrt{3/2}B_m m_0^{(2)}\right] + m_{\pm 1}^{(2)}\Gamma = 0. \tag{A1c}$$

The subsequent steady-state solution $m_{\mathrm{Hanle},q}^{(2)}$ is

$$m_{\mathrm{Hanle},0}^{(2)} = \frac{\Gamma_p\left(\Gamma^2 - 2\gamma^2 B_z^2 + \gamma^2 B_m^2 + 3i\gamma B_z\Gamma\right)\left(\Gamma^2 - 2\gamma^2 B_z^2 + \gamma^2 B_m^2 - 3i\gamma B_z\Gamma\right)}{\sqrt{6}\Gamma\left(\gamma^2 B_z^2 + \gamma^2 B_m^2 + \Gamma^2\right)\left(4\gamma^2 B_z^2 + 4\gamma^2 B_m^2 + \Gamma^2\right)}, \tag{A2a}$$

$$m_{\mathrm{Hanle},\pm 2}^{(2)} = -\frac{\gamma^2 B_m^2 \Gamma_p\left(\Gamma^2 - 2\gamma^2 B_z^2 + \gamma^2 B_m^2 \pm 3i\gamma B_z\Gamma\right)}{2\Gamma\left(\gamma^2 B_z^2 + \gamma^2 B_m^2 + \Gamma^2\right)\left(4\gamma^2 B_z^2 + 4\gamma^2 B_m^2 + \Gamma^2\right)}, \tag{A2b}$$

$$m_{\mathrm{Hanle},\pm 1}^{(2)} = \pm\frac{\gamma B_m \Gamma_p\left(\Gamma^2 - 2\gamma^2 B_z^2 + \gamma^2 B_m^2 \pm 3i\gamma B_z\Gamma\right)\left(2\gamma B_z \pm i\Gamma\right)}{2\Gamma\left(\gamma^2 B_z^2 + \gamma^2 B_m^2 + \Gamma^2\right)\left(4\gamma^2 B_z^2 + 4\gamma^2 B_m^2 + \Gamma^2\right)}. \tag{A2c}$$

[1] E. Boto, N. Holmes, J. Leggett, G. Roberts, V. Shah, S. S. Meyer, L. D. Muñoz, K. J. Mullinger, T. M. Tierney, S. Bestmann, G. R. Barnes, R. Bowtell, and M. J. Brookes, Moving magnetoencephalography towards real-world applications with a wearable system, Nature (London) **555**, 657 (2018).

[2] C. Abel *et al.*, Measurement of the Permanent Electric Dipole Moment of the Neutron, Phys. Rev. Lett. **124**, 081803 (2020).

[3] N. Olsen, G. Hulot, and T. Sabaka, Measuring the earth's magnetic field from space: Concepts of past, present and future missions, Space Sci. Rev. **155**, 65 (2010).

[4] A. Balogh, Planetary magnetic field measurements: Missions and instrumentation, Space Sci. Rev. **152**, 23 (2010).

[5] D. Budker and M. Romalis, Optical magnetometry, Nat. Phys. **3**, 227 (2007).

[6] A. Weis, G. Bison, and A. S. Pazgalev, Theory of double resonance magnetometers based on atomic alignment, Phys. Rev. A **74**, 033401 (2006).

[7] Z. D. Grujić and A. Weis, Atomic magnetic resonance induced by amplitude-, frequency-, or polarization-modulated light, Phys. Rev. A **88**, 012508 (2013).

[8] I. K. Kominis, T. W. Kornack, J. C. Allred, and M. V. Romalis, A subfemtotesla multichannel atomic magnetometer, Nature (London) **422**, 596 (2003).

[9] S. J. Seltzer and M. V. Romalis, Unshielded three-axis vector operation of a spin-exchange-relaxation-free atomic magnetometer, Appl. Phys. Lett. **85**, 4804 (2004).

[10] H. Huang, H. Dong, L. Chen, and Y. Gao, Single-beam three-axis atomic magnetometer, Appl. Phys. Lett. **109**, 062404 (2016).

[11] N. Castagna and A. Weis, Measurement of longitudinal and transverse spin relaxation rates using the ground-state Hanle effect, Phys. Rev. A **84**, 053421 (2011).

[12] E. Breschi and A. Weis, Ground-state Hanle effect based on atomic alignment, Phys. Rev. A **86**, 053427 (2012).

[13] R. E. Slocum and F. N. Reilly, Low field helium magnetometer for space applications, IEEE Trans. Nucl. Sci. **10**, 165 (1963).

[14] G. Le Gal, G. Lieb, F. Beato, T. Jager, H. Gilles, and A. Palacios-Laloy, Dual-Axis Hanle Magnetometer Based on Atomic Alignment with a Single Optical Access, Phys. Rev. Appl. **12**, 064010 (2019).

[15] J. Dupont-Roc, S. Haroche, and C. Cohen-Tannoudji, Detection of very weak magnetic fields (10^{-9} gauss) by ^{87}Rb zero-field level crossing resonances, Phys. Lett. A **28**, 638 (1969).

[16] R. E. Slocum, Zero-Field Level-Crossing Resonances in Optically Pumped 2^3S_1 He^4, Phys. Rev. Lett. **29**, 1642 (1972).

[17] N. Polonsky and C. Cohen-Tannoudji, Interprétation quantique de la modulation de fréquence, J. Phys. France **26**, 409 (1965).

[18] C. Cohen-Tannoudji and S. Haroche, Absorption et diffusion de photons optiques par un atome en interaction avec des photons de radiofréquence, J. Phys. France **30**, 153 (1969).

[19] C. Cohen-Tannoudji, J. Dupont-Roc, S. Haroche, and F. Laloë, Diverses résonances de croisement de niveaux sur des atomes pompés optiquement en champ nul. I. Théorie, Rev. Phys. Appl. (Paris) **5**, 95 (1970).

[20] C. Cohen-Tannoudji, J. Dupont-Roc, S. Haroche, and F. Laloë, Diverses résonances de croisement de niveaux sur des atomes pompés optiquement en champ nul II. Applications à la mesure de champs faibles, Rev. Phys. Appl. (Paris) **5**, 102 (1970).

[21] J. Dupont-Roc, Étude théorique de diverses résonances observables en champ nul sur des atomes "habillés" par des photons de radiofréquence, J. Phys. France **32**, 135 (1971).

[22] F. Beato, E. Belorizky, E. Labyt, M. Le Prado, and A. Palacios-Laloy, Theory of a ^{4}He parametric-resonance magnetometer based on atomic alignment, Phys. Rev. A **98**, 053431 (2018).

[23] J. Dupont-Roc, Détermination par des méthodes optiques des trois composantes d'un champ magnétique très faible, Rev. Phys. Appl. (Paris) **5**, 853 (1970).

[24] F. Bertrand, T. Jager, A. Boness, W. Fourcault, G. Le Gal, A. Palacios-Laloy, J. Paulet, and J. M. Léger, A

^{4}He vector zero-field optically pumped magnetometer operated in the Earth-field, Rev. Sci. Instrum. **92**, 105005 (2021).

[25] E. Labyt, M.-C. Corsi, W. Fourcault, A. Palacios-Laloy, F. Bertrand, F. Lenouvel, G. Cauffet, M. Le Prado, F. Berger, and S. Morales, Magnetoencephalography with optically pumped ^{4}He magnetometers at ambient temperature, IEEE Trans. Med. Imaging **38**, 90 (2019).

[26] S. Morales, M.-C. Corsi, W. Fourcault, F. Bertrand, G. Cauffet, C. Gobbo, F. Alcouffe, F. Lenouvel, M. Le Prado, F. Berger, G. Vanzetto, and E. Labyt, Magnetocardiography measurements with ^{4}He vector optically pumped magnetometers at room temperature, Phys. Med. Biol. **62**, 7267 (2017).

[27] J. Tang, Y. Zhai, B. Zhou, B. Han, and G. Liu, Dual-axis closed loop of a single-beam atomic magnetometer: Toward high bandwidth and high sensitivity, IEEE Trans. Instrum. Meas. **70**, 1 (2021).

[28] W. Fourcault, R. Romain, G. Le Gal, F. Bertrand, V. Josselin, M. Le Prado, E. Labyt, and A. Palacios-Laloy, Helium-4 magnetometers for room-temperature biomedical imaging: Toward collective operation and photon-noise limited sensitivity, Opt. Express **29**, 14467 (2021).

[29] T. Yabuzaki, N. Tsukada, and T. Ogawa, Modification of atomic *g*-factor by the oscillating rf field, J. Phys. Soc. Jpn. **32**, 1069 (1972).

[30] Z. Li, R. T. Wakai, and T. G. Walker, Parametric modulation of an atomic magnetometer, Appl. Phys. Lett. **89**, 134105 (2006).

[31] Z. Ding, J. Yuan, G. Lu, Y. Li, and X. Long, Three-axis atomic magnetometer employing longitudinal field modulation, IEEE Photon. J. **9**, 5300209 (2017).

[32] J. Wang, W. Fan, K. Yin, Y. Yan, B. Zhou, and X. Song, Combined effect of pump-light intensity and modulation field on the performance of optically pumped magnetometers under zero-field parametric modulation, Phys. Rev. A **101**, 053427 (2020).

[33] G. Le Gal, L.-L. Rouve, and A. Palacios-Laloy, Parametric resonance magnetometer based on elliptically polarized light yielding three-axis measurement with isotropic sensitivity, Appl. Phys. Lett. **118**, 254001 (2021).

[34] D. Budker, W. Gawlik, D. F. Kimball, S. M. Rochester, V. V. Yashchuk, and A. Weis, Resonant nonlinear magneto-optical effects in atoms, Rev. Mod. Phys. **74**, 1153 (2002).

[35] F. Beato and A. Palacios-Laloy, Second-order effects in parametric-resonance magnetometers based on atomic alignment, EPJ Quantum Technol. **7**, 9 (2020).

[36] A. Omont, Irreducible components of the density matrix. Application to optical pumping, Prog. Quantum Electron. **5**, 69 (1977).

[37] M. K. Plante, A generalized theory of double-resonance laser-pumped helium-4 magnetometers, Ph.D. thesis, The University of Texas at Dallas, 2010.

[38] Y. Shi, T. Scholtes, Z. D. Grujić, V. Lebedev, V. Dolgovskiy, and A. Weis, Quantitative study of optical pumping in the presence of spin-exchange relaxation, Phys. Rev. A **97**, 013419 (2018).

[39] C. Cohen-Tannoudji, Atomes "habillés" par des photons ou de radiofréquence, J. Phys. Colloq. **32**, C5–11 (1971).

[40] C. Landré, C. Cohen-Tannoudji, J. Dupont-Roc, and S. Haroche, Anisotropie des propriétés magnétiques d'un atome "habillé" par des photons de RF, J. Phys. France **31**, 971 (1970).

[41] F. Laloë, M. Leduc, and P. Minguzzi, Relations entre l'état angulaire d'une vapeur atomique soumise au pompage optique et ses propriétés d'absorption et de dispersion. - Première Partie, J. Phys. France **30**, 277 (1969).

[42] W. Xiao, H. Wang, X. Zhang, Y. Wu, T. Wu, J. Chen, X. Peng, and H. Guo, In situ calibration of magnetic field coils using parametric resonance in optically-pumped magnetometers, in *2021 Joint Conference of the European Frequency and Time Forum and IEEE International Frequency Control Symposium (EFTF/IFCS)* (IEEE, Gainesville, FL, 2021), pp. 1–3.